

See discussions, stats, and author profiles for this publication at: <https://www.researchgate.net/publication/200051121>

Understanding the Dielectric Properties of Heat-Treated Carbon Nanofibers at Terahertz Frequencies: a New Perspective on the Catalytic Activity of Structured Carbonaceous Materials

ARTICLE in THE JOURNAL OF PHYSICAL CHEMISTRY C · MAY 2009

Impact Factor: 4.77 · DOI: 10.1021/jp811226d

CITATIONS

25

READS

6

10 AUTHORS, INCLUDING:



J. Axel Zeitler

University of Cambridge

144 PUBLICATIONS 2,272 CITATIONS

SEE PROFILE



James McGregor

The University of Sheffield

41 PUBLICATIONS 570 CITATIONS

SEE PROFILE



Husnu Emrah Unalan

Middle East Technical University

85 PUBLICATIONS 1,835 CITATIONS

SEE PROFILE



Jean-Philippe Tessonnier

Iowa State University

85 PUBLICATIONS 1,969 CITATIONS

SEE PROFILE

Understanding the Dielectric Properties of Heat-Treated Carbon Nanofibers at Terahertz Frequencies: a New Perspective on the Catalytic Activity of Structured Carbonaceous Materials

Edward P. J. Parrott,^{†,‡} J. Axel Zeitler,[‡] James McGregor,[‡] Shu-Pei Oei,[§] Husnu Emrah Unalan,[§] Swee-Ching Tan,[¶] William I. Milne,[§] Jean-Philippe Tessonier,^{||} Robert Schlögl,^{||} and Lynn F. Gladden^{*,‡}

Department of Physics, Cavendish Laboratory, University of Cambridge, J. J. Thomson Avenue, Cambridge CB3 0HE, United Kingdom, Department of Chemical Engineering and Biotechnology, University of Cambridge, Pembroke Street, Cambridge CB2 3RA, United Kingdom, Centre for Advanced Photonics and Electronics, University of Cambridge, J. J. Thomson Avenue, Cambridge CB3 0FA, United Kingdom, University of Cambridge Nanoscience Centre, J. J. Thomson Avenue, Cambridge CB3 0FF, United Kingdom, and Fritz-Haber-Institut der Max-Planck-Gesellschaft, Berlin D-14195, Germany

Received: December 19, 2008; Revised Manuscript Received: April 24, 2009

Terahertz time domain spectroscopy (THz-TDS) has been used to study the electrical and optical properties of a series of carbon nanofibers (CNFs) that have undergone different heat treatments. The high-temperature heat-treated (HHT) sample displayed increased absorption and real refractive indices across the range 0.3–3.5 THz when compared to the low-temperature heat-treated (LHT) and pyrolytically stripped (PS) samples. The experimental results were fitted by using a Drude–Lorentz model and an effective medium approximation to yield the electrical parameters of the sample such as the plasma frequency, phonon mode frequency, and oscillator strength. These parameters were used to rationalize the differences as being due to an increase in graphitic order in the HHT sample when compared to the LHT sample and to an even greater extent the PS sample. HHT, LHT, and PS CNFs can be used as catalysts for the oxidative dehydrogenation of ethylbenzene to styrene. They exhibit different catalytic yield and selectivity which can be correlated with their dielectric properties at terahertz frequencies. The results suggest that THz-TDS is a useful tool for characterizing the graphiticity of CNFs in terms of electron density and mobility which, in turn, correlate with the catalytic performance of these materials.

Introduction

In recent years THz-TDS has been used in an increasing number of fields, including studies of pharmaceuticals,¹ DNA,² proteins,³ and carbon nanotubes (CNTs).^{4–7} THz-TDS has been found to be of great use in the investigation of CNTs as it allows the frequency-dependent electrical and optical parameters of the nanotubes to be calculated without the need of the Kramers–Krönig relationship (which has to be used in FTIR spectroscopy, for example). This is possible because the time domain waveform contains both magnitude and phase information which may be extracted by using a Fast Fourier Transform (FFT). By using a combination of the Drude–Lorentz (DL) and effective medium approximation (EMA) models it has previously been demonstrated that it is possible to interpret the differences between “pristine” CNTs and hydrogen-functionalized CNTs solely in terms of a change in plasma frequency of the DL model.⁵ This suggested that there was an increased number of charge carriers in pristine CNTs compared to the functionalized CNTs, resulting in an increase in the absorption coefficient and real refractive index of the pristine CNTs.

CNTs and CNFs have a wide range of potential applications, including electronics, composite materials, drug delivery, hydrogen storage, and uses in heterogeneous catalysis.⁸ Carbonaceous materials in catalysis are most commonly associated with catalyst deactivation; however, highly ordered carbon structures have been shown to exhibit high activity and selectivity in a number of reactions. For instance, onion-like carbon structures exhibited high yields and selectivity in the oxidative dehydrogenation (ODH) of ethylbenzene.⁹ In that work the activity of the nanostructured carbons was related to their degree of graphitic order. Specifically, materials with a higher basal plane to edge/kink site ratio (i.e., less ordered materials) provided higher yields of styrene. The activity of carbonaceous materials for ethylbenzene ODH has been investigated by a number of workers.^{10–14} The characterization of such ordered carbonaceous materials represents a significant challenge for traditional optical spectroscopies (e.g., due to high absorption) and ¹³C NMR spectroscopy, which is unsuitable for conducting or paramagnetic samples.^{15–17} In the present study we have investigated the catalytic activity of a series of heat-treated CNFs for ethylbenzene ODH, and attributed differences in activity to their electrical and physical properties as revealed by THz-TDS. Given that the heat treatment process is expected to remove or graphitize the layer of disordered carbon that envelops CNFs,^{18,19} this paper explores the extent to which THz-TDS can be used to probe the electron landscape in these materials. We present models of the measured dielectric response in terms of the

* To whom correspondence should be addressed. E-mail: gladden@cheng.cam.ac.uk.

[†] Department of Physics, Cavendish Laboratory, University of Cambridge.

[‡] Department of Chemical Engineering and Biotechnology, University of Cambridge.

[§] Centre for Advanced Photonics and Electronics, University of Cambridge.

[¶] University of Cambridge Nanoscience Centre.

^{||} Fritz-Haber-Institut der Max-Planck-Gesellschaft.

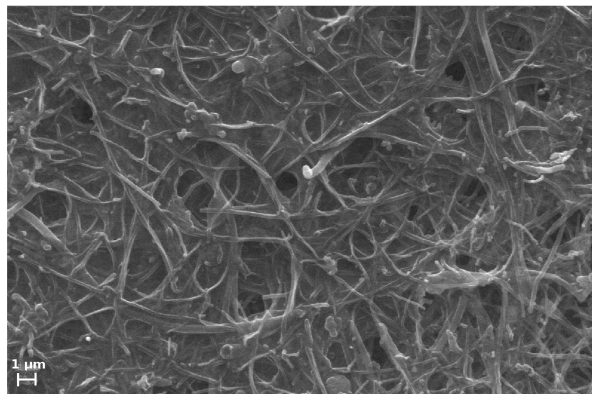


Figure 1. Scanning electron micrograph of the film surface of the PS sample.

availability of charge carriers in the different CNF samples and relate these to the observed trend in catalytic selectivity.

Experimental Section

The sample materials PR19XT-PS, PR19XT-LHT, and PR19XT-HHT were sourced commercially (Pyrograf-III, Pyrograf Products Inc., Cedarville, OH). These samples have been described in detail in the literature^{18,19} and have a measured diameter of 108 ± 47 nm. The PS sample has been pyrolytically stripped at 973 K in order to remove any polyaromatic hydrocarbons from the CNF surface. In contrast, the LHT sample has been treated at 1773 K in order to carbonize and chemically vaporize deposited amorphous carbon while the HHT sample has been treated at the higher temperature of 3273 K resulting in the graphitization of the CNF.²⁰ Further preparation details are documented elsewhere.¹⁸ Vapor grown CNF thin films were prepared by using the vacuum filtration method.²¹ Briefly, aqueous dispersions of the CNF samples at a concentration of 2 mg/L were prepared through sonication in 2-propanol. CNF films of different densities and thicknesses were achieved by filtration of volumes of either 50 or 80 mL through 220 nm pore size Millipore mixed cellulose ester membranes. The ester membrane with the CNF thin film was then transferred onto a z-cut quartz disks, compressively loaded, heated to 343 K by a hot plate, and etched in consecutive acetone and 2-propanol baths, leaving behind CNF thin films on the substrates for measurements. Due to the preparation method the fibers were randomly aligned parallel to the substrate (see Figure 1). The films had thicknesses between 3 and 10 μm . Thickness measurements were performed with a Dektak 6 M profilometer (Veeco Instruments Inc., Woodbury NY).

Catalytic activity tests were carried out with a quartz microreactor. A fixed bed of CNF (0.1 cm^3) was constrained between two plugs of quartz wool and held isothermally at 773 K. The reaction mixture, ethylbenzene, oxygen, and nitrogen in a 3.7:4.8:91.5 ratio, was introduced at a flow rate of $50 \text{ cm}^3 \text{ min}^{-1}$, with a total pressure inside the reactor of 2.7×10^5 Pa. The reaction products were analyzed by using a gas chromatograph (Agilent 6890 GC), employing a flame ionization detector. The results are reported in terms of the styrene yield, $100 \times (\text{mol styrene produced})/(\text{mol ethylbenzene fed})$, with selectivity indicated by the ratio of styrene to other hydrocarbon products, $(\text{mol styrene produced})/(\text{mol other hydrocarbon products})$. These quantities have previously been used to indicate the catalytic performance of carbonaceous materials in this reaction.²²

THz-TDS was performed at 293 K with a setup similar to that described previously.²³ To speed up the acquisition process,

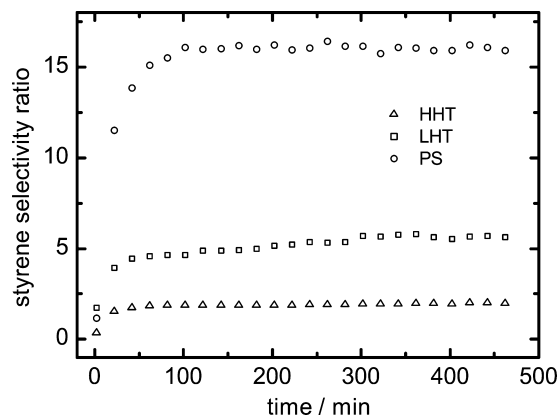


Figure 2. Ratio of styrene to other hydrocarbon products as a function of time on stream.

and to improve spectral resolution and signal-to-noise ratio, a 50 ps rapid optical delay was used. For each time domain waveform, 200 scans were coadded. After averaging, the waveforms were truncated at 30 ps to avoid a source reflection and zero filled to the next power of 2. FFT was performed to extract the magnitude and phase of the signal as a function of frequency. For each sample a time domain waveform was acquired through the sample film on the substrate as well as the substrate only. The substrate-only time domain waveform was used as the reference waveform in the subsequent analysis.

Results and Discussion

Catalytic activity tests were carried out on the three CNF samples. ODH of ethylbenzene results in the formation of a variety of hydrocarbon products, with styrene and benzene accounting for in excess of 96% of these in all cases. The ratio of styrene to other hydrocarbon products is shown in Figure 2. After 8 h on stream this value is 15.9, 5.6, and 2.0 for PS, LHT, and HHT samples, respectively. Considering the yield of styrene over the three materials the same trend is observed, with yields of 31.3%, 26.1%, and 20.5% obtained at this time. A previous study compared the activity of onion-like carbon (OLC) and ultradispersed diamond (UDD) for ethylbenzene dehydrogenation.²² In that work a styrene-to-benzene ratio of approximately 30:1 was achieved over OLC in contrast to only approximately 3:1 over UDD; it was proposed that quinolinic functionalities, which are believed to be the source of selectivity toward styrene, are more easily formed at the surface of OLC. These functionalities are formed in situ during reaction. The ranking of the CNFs with respect to selectivity to styrene in the present study suggests that the ease of forming quinolinic functionalities is most likely greatest on PR19XT-PS, followed by PR19XT-LHT and finally PR19XT-HHT.

Quinolinic functionalities will most easily form at defect sites, and therefore selectivity might be expected to correlate inversely with graphiticity, and thus with the free electron density within the CNFs. Such structural and electronic properties of the catalytic materials can be probed by THz-TDS. In the THz-TDS experiments the frequency-dependent magnitude and phase information extracted for each sample and reference was analyzed as follows to extract the dielectric properties of the sample. By considering the sample as a thin film (refractive index \tilde{n}_1) deposited on a quartz substrate (refractive index \tilde{n}_2) the following equation relating the complex frequency spectrum of the sample A_{sam} with that of the reference (quartz only) A_{ref} is derived. This is achieved by summing the reflections within the thin film between the quartz and air (refractive index \tilde{n}_0)

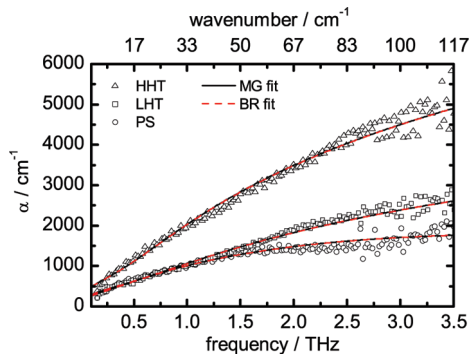


Figure 3. Absorption coefficient plotted for the three CNF samples. The solid and dotted lines are the absorption spectra calculated by using the Drude–Lorentz model combined with two effective medium approximation models (Maxwell–Garnett and Bruggeman).

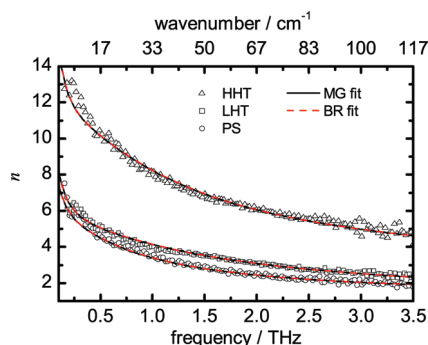


Figure 4. Real refractive index plotted for the three CNF samples. The solid and dotted lines are the real refractive indices calculated by using the Drude–Lorentz model combined with two effective medium approximation models (Maxwell–Garnett and Bruggeman).

interfaces:

$$\frac{A_{\text{sam}}(\omega)}{A_{\text{ref}}(\omega)} = \frac{t_{01}t_{12}\exp(i\beta)\exp(-i\beta_0)}{t_{02}(1 + r_{01}r_{12}\exp(i2\beta))} \quad (1)$$

where t_{01} , r_{01} , t_{12} , and r_{12} are the Fresnel transmission and reflection coefficients from air into the sample and from the sample into the substrate, respectively, and t_{02} is the transmission coefficient from air into the substrate. $\beta_0 (=d\omega/c)$ accounts for the displacement of the air from the sample compared to the reference waveform due to the thin film and $\beta (= \tilde{n}d\omega/c)$ is the propagation vector through the thin film (d is the thin film thickness). β is related to the complex refractive index \tilde{n} :

$$\tilde{n}(\omega) = n(\omega) + ik(\omega) = \sqrt{\varepsilon(\omega)} \quad (2)$$

where $\varepsilon(\omega)$ is the complex dielectric function of the material. Equation 1 represents the theoretical model for the comparison of the reference and sample spectra, therefore if the thickness of the thin film is known, the complex refractive index of the sample may be obtained by minimizing the difference between the experimental ratio of the sample spectrum to the reference spectrum and the theoretical ratio as predicted by using eq 1. The minimum function found in this way uses the theoretical ratio with the best estimates of the complex refractive index of the sample. Figures 3 and 4 show the absorption coefficient and real refractive index of the samples calculated with this approach.

As seen in Figures 3 and 4, PS, LHT, and HHT samples each have significantly different responses with respect to both absorption coefficient and real refractive index as a function of frequency. Differences in the shape of the absorption spectra were observed between the three samples, with a progressively increasing gradient detected from the PS to LHT and HHT sample. This has resulted in an increased absorption coefficient for the two samples treated at higher temperatures, particularly at higher frequencies. For example, the absorption coefficient at 2 THz for the PS, LHT, and HHT samples is 1480, 1890, and 3500 cm^{-1} , respectively. The real refractive index also shows a large difference between the HHT sample and the LHT and PS samples with the HHT sample displaying a much higher refractive index throughout the frequency range. The difference between the LHT sample and the PS sample is less pronounced but the sample treated at higher temperature has a higher refractive index, especially above 1 THz. For example, the real refractive index observed at 2 THz for the PS, LHT, and HHT samples is 2.4, 3.1, and 6.0, respectively.

Further understanding of the differences in structural and electrical characteristics between the three samples has been achieved by modeling the dielectric response of the samples by using an EMA and the DL model following the method reported in a recent investigation of CNTs.⁵ The DL model considers the dielectric response of the CNFs (ε_{CNF}) as a combination of three terms: the background permittivity (ε_{∞}), the free electron response (the Drude term), and the contribution of bound electrons within the carbon structure that oscillate at particular vibrational frequencies or phonon modes (the Lorentz term). As such it takes the following form:

$$\varepsilon_{\text{CNF}}(\omega) = \varepsilon_{\infty} - \frac{\Omega_p^2}{\omega^2 + i\Gamma\omega} + \sum_k \frac{\Omega_{p,k}^2}{(\omega_k^2 - \omega^2) - i\Gamma_k\omega} \quad (3)$$

where Ω_p is the Drude plasma frequency, Γ is the Drude damping rate, and $\Omega_{p,k}$, ω_k , and Γ_k are the Lorentz plasma frequency (commonly known as the oscillator strength), phonon frequency, and the spectral width respective to the k -th Lorentzian mode. The use of a single Lorentz mode was found to give an adequate fit to the observed data within the spectral region of interest. The plasma frequency for the Drude term is of the following form:

$$\Omega_p = \sqrt{\frac{N_e e^2}{m_e \varepsilon_0}} \quad (4)$$

As can be seen in eq 4 the plasma frequency is proportional to the square root of the number of electrons available to that interaction (N_e); therefore the Drude plasma frequency will be proportional to the square root of the free-electron density. An analogous form of eq 4 exists for the Lorentz plasma frequency, where N_e refers to the number of bound electrons available to the interaction; therefore the plasma frequency of the Lorentz modes will be proportional to the square root of the bound-electron density corresponding to that oscillation energy. The Drude damping rate also has a clear relationship to the free-electron density due to its relationship with the free-electron collision rate, τ :

$$\Gamma = \frac{1}{\tau} = N_e v \sigma \quad (5)$$

where v is the electron drift velocity and σ is the scattering cross section. Equation 5 therefore suggests that an increase in the Drude damping rate (Γ) can be correlated with an increase in the free-electron density. Possible physical interpretations of the Lorentzian spectral width (Γ_k) are more difficult. As with the Drude damping rate this term is a retarding term on the phonon mode oscillation; however, Γ_k is likely to be influenced by contributions from both the bound and free electron densities.

Two EMAs were implemented to model the dielectric constant of the resulting thin film as a combination of the dielectric constant of the CNFs as modeled in eq 3 with a host medium in this case assumed to be air with a dielectric constant of 1. They are known as the Maxwell–Garnett (MG) and Bruggeman (BR) models and are as follows:

$$\text{Maxwell-Garnett: } (1 - f) \frac{\epsilon_{\text{sub}} - \epsilon_{\text{CNF}}}{\epsilon_{\text{sub}} + 2\epsilon_{\text{CNF}}} = \frac{\epsilon_{\text{eff}} - \epsilon_{\text{CNF}}}{\epsilon_{\text{eff}} + 2\epsilon_{\text{CNF}}} \quad (6)$$

$$\text{Bruggeman: } f \frac{\epsilon_{\text{CNF}} - \epsilon_{\text{eff}}}{\epsilon_{\text{CNF}} + 2\epsilon_{\text{eff}}} + (1 - f) \frac{\epsilon_{\text{sub}} - \epsilon_{\text{eff}}}{\epsilon_{\text{sub}} + 2\epsilon_{\text{eff}}} = 0 \quad (7)$$

where ϵ_{eff} , ϵ_{CNF} , and ϵ_{sub} are the dielectric constants of the effective medium, CNFs, and host dielectric, respectively, and f is the volume density of the CNFs as a fraction of the whole medium. The two effective medium models are shown schematically in Figure 5. Figure 5a describes the essential features of the MG model. The hashed region represents the pseudoparticle with the effective dielectric constant (ϵ_{eff}), which is composed of the host dielectric and the inclusions (ϵ_{CNF}). The polarizability of this pseudoparticle within the host dielectric is modeled as the sum of the polarizabilities of the inclusions within the host dielectric that are contained within the volume of the pseudoparticle. In contrast, in the BR model (Figure 5b), the total polarization of the region is found by considering the polarizabilities of the inclusion particles (ϵ_{CNF}) and host dielectric particles embedded within a medium. For the effective dielectric constant to be the dielectric constant of this medium the polarizabilities of the embedded particles must sum to zero. These subtle differences in how the models treat the substrate and inclusions means that the MG model is not necessarily as applicable as the BR model for high concentrations of polarized particles. However, little difference was observed between the two models for these samples as is shown in Table 1. For clarity only the values for the MG model are discussed within the text. It should be noted that in eqs 6 and 7 the CNF orientation has been assumed to be isotropic within the thin film to simplify the model.

Table 1 contains the parameters of the models used to produce the best fit lines in Figures 3 and 4. By using a high-resolution Scanning Electron Microscope (SEM) (Carl Zeiss EVO 50) running at 20 kV to image the thin film surface and subsequent image analysis, a lower bound to the filling factor was found to be ~ 0.7 (Figure 1). This agreed well with the filling factors extracted from the models which were 0.75 for the PS and LHT samples and 0.9 for the HHT sample. The single phonon mode frequency ($\omega_{0,j}$, at ~ 7.0 THz) obtained from the analysis did not vary significantly between the three samples and correlates

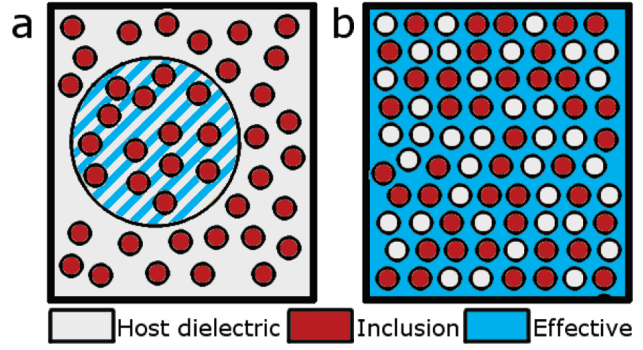


Figure 5. Schematic of the (a) Maxwell–Garnett (MG) and (b) Bruggeman (BR) models used as an Effective Medium Approximation (EMA). In the above key, the inclusion refers to the CNFs.

TABLE 1: Fitting Parameters (in THz) for the Maxwell–Garnett and Bruggeman Models Fitted to the Experimental Data and Shown in Figures 3 and 4

		$\Omega_p/2\pi$	$\Gamma/2\pi$	$\Omega_{p,j}/2\pi$	$\omega_{0,j}/2\pi$	$\Gamma_j/2\pi$	f	ϵ_∞
PS	MG	8.30	5.13	36.0	6.91	84.7	0.75	4.0
	BR	8.32	4.86	36.9	6.90	84.2	0.75	4.0
LHT	MG	16.1	16.4	36.1	6.93	48.3	0.78	2.0
	BR	16.0	14.1	39.1	7.01	49.5	0.75	2.0
HHT	MG	57.6	84.6	73.6	7.08	60.1	0.90	7.6
	BR	60.5	87.4	76.7	7.14	61.1	0.87	8.0

well with the lowest infrared active phonon mode calculated for a CNT system, and so we postulate that this is a graphitic vibrational mode of the CNF. The values reported here are slightly lower than those reported in earlier studies of CNTs,²⁴ most likely a result of the increased diameter of the CNFs studied in the work reported here. The clearest insight into the properties of the CNFs is found by considering the plasma frequency (Ω_p) and the Drude damping rate (Γ), where an increase in both terms is observed when going from the PS sample through the LHT sample to the HHT sample. The plasma frequency is proportional to the square root of the free electron density and so an increase in this value from 8.3 THz in the PS sample to 16.1 THz in the LHT sample and then 57.6 THz in the HHT sample is indicative of an increased number of free electrons within the higher heat-treated samples in comparison to the PS sample. Consistent with this result, the Drude damping rate, which is related to the electron collision rate,⁴ shows an increase in value from 5.13 THz in the PS sample to 16.4 THz in the LHT sample and 84.6 THz in the HHT sample corresponding to an increase in the density of free electrons as the temperature of the heat treatment increases. A change is also observed in the Lorentz oscillator strength ($\Omega_{p,j}$), especially between the HHT and LHT/PS samples. The Lorentz oscillator strength is indicative of the number of electrons in the bound state with the corresponding resonant frequency, and so if this resonant frequency corresponds to a graphitic CNT/CNF vibrational mode as has been postulated herein, the Lorentz oscillator strength could be thought of as a measure of the graphitic order of the sample. Therefore, the model values fitted may indicate a more substantial region of graphene-type order within the HHT sample ($\Omega_{p,j} = 73.6$ THz) when compared to both the LHT sample and the PS sample ($\Omega_{p,j} = 36.1$ and 36.0 THz, respectively), and a corresponding decrease in the number of defect sites. The change in all three of these parameters implies that there has been an increase in the graphiticity of the HHT sample, and to an extent the LHT sample, when compared to that of the PS sample. The results reported herein suggest that an overall increase in the terahertz absorption

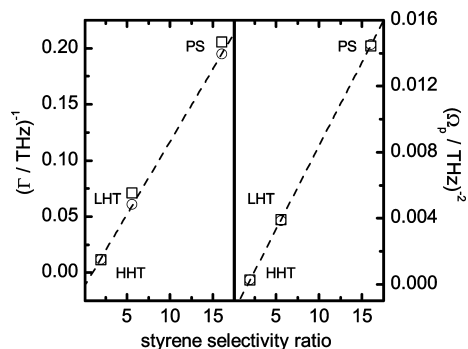


Figure 6. Correlations of Ω_p and Γ with the selectivity of styrene to other hydrocarbon products for the three CNF samples: circles, Maxwell–Garnett model parameters; squares, Bruggeman model parameters.

corresponds to increasing structural order and loss of functionality, in good agreement with previous conclusions from THz-TDS studies of functionalized CNTs.⁵ The increased absorption coefficient and real refractive index (Figures 3 and 4), when comparing PS, LHT, and HHT in the present study, would therefore imply that there is a trend toward a greater number of charge carriers and fewer defect sites present as treatment temperature is increased.

Upon closer analysis of the plasma frequency (Ω_p) and the Drude damping rate (Γ) it is interesting to note that the inverse square of Ω_p and the inverse of Γ , extracted from the model fits for the terahertz dielectric values discussed above, both exhibit linear correlations with respect to the selectivity to styrene in the ODH reaction over the three samples (see Figure 6). These correlations are also self-consistent as both Ω_p^2 and Γ are directly proportional to the free electron density (which is itself inversely proportional to the free electron mobility μ due to electron–electron interactions). This may be indicative of a loss of the functional groups such as quinoline moieties (in analogy with the hydrogen functionalization reported previously)⁵ which have been proposed to be the catalytic centers for styrene production.²² The observed trend in styrene selectivity ratio and yield for ethylbenzene oxidative dehydrogenation of PS > LHT > HHT can therefore be explained by the differences in the structural and electrical properties of the CNFs. This is supported by previous studies which have proposed that catalytic activity is linked to the number of defect sites within the polyconjugated carbon network.⁹

The characterization of the CNFs by THz-TDS in the present work has allowed their catalytic performance to be correlated directly with their graphitic character and hence the ease with which catalytically active sites are formed. Traditional techniques such as Raman spectroscopy have been qualitatively used to identify the amount of disorder and graphitisation in CNFs.^{25–27} In addition to this function, the implementation of THz-TDS allows for the characterization of the electron mobility and defect density of CNFs which may offer useful insights into the catalytic activity of these fibers.

Conclusions

In this paper we have used THz-TDS and the DL model combined with EMA theory to record and explain the differences in three samples of CNFs heat treated at progressively higher temperatures. These differences have then been related to the catalytic performance of the CNFs in the oxidative dehydrogenation of ethylbenzene. THz-TDS recorded much higher absorption coefficients and real refractive indices in the CNFs

treated at the higher temperatures. Application of the DL model and an EMA indicated an increase in the plasma frequency, Drude damping rate, and oscillator strength suggesting that the HHT sample, and to a lesser extent the LHT sample, had a higher mobile electron density and a more substantial region of graphene-like order when compared to the PS sample. Catalytic studies of the samples produced results consistent with this hypothesis, with the least graphitic sample (the PS sample) recording the highest styrene yield, followed by the LHT and HHT samples. This sensitivity to changes in the electrical properties of such graphitic structures makes THz-TDS an ideal tool to understand the physical and electrical properties of these materials. These data can then be used to gain insights into their catalytic properties as a function of electron mobility and defect density. Indeed, in circumstances where traditional approaches such as NMR can no longer be used due to the increasing conductivity of the sample, terahertz may give valuable new insights to the catalytic performance of such systems.

Acknowledgment. The authors would like to thank the following sources of funding: ATHENA project funded by the EPSRC and Johnson Matthey plc. (GR/R47523/01, J.McG., L.F.G.), EPSRC and RCUK Basic Technology Grant (EP/E048811/1, E.P.J.P., J.A.Z., L.F.G.), and ECFP6 DESYGN- IT (S.-P.O., H.E.U., S.-C.T., W.I.M.).

Supporting Information Available: A figure of the simulated absorption coefficients from 0.3 to 15 THz for each sample as produced by the MG model parameters in Table 1. This material is available free of charge via the Internet at <http://pubs.acs.org>.

References and Notes

- (1) Zeitler, J. A.; Taday, P. F.; Newnham, D. A.; Pepper, M.; Gordon, K. C.; Rades, T. *J. Pharm. Pharmacol.* **2007**, *59*, 209–223.
- (2) Fischer, B. M.; Walther, M.; Jepsen, P. U. *Phys. Med. Biol.* **2002**, *47*, 3807–3814.
- (3) Markelz, A.; Roitberg, A.; Heilweil, E. J. *Chem. Phys. Lett.* **2000**, *320*, 42–48.
- (4) Jeon, T. I.; Son, J. H.; An, K. H.; Lee, Y. H.; Lee, Y. S. *J. Appl. Phys.* **2005**, *98*, 034316.
- (5) Kang, C.; Maeng, I. H.; Oh, S. J.; Lim, S. C.; An, K. H.; Lee, Y. H.; Son, J. H. *Phys. Rev. B* **2007**, *75*, 085410.
- (6) Maeng, I.; Kang, C.; Oh, S. J.; Son, J. H.; An, K. H.; Lee, Y. H. *Appl. Phys. Lett.* **2007**, *90*, 051914.
- (7) Nishimura, H.; Minami, N.; Shimano, R. *Appl. Phys. Lett.* **2007**, *91*, 011108.
- (8) Serp, P.; Corrias, M.; Kalck, P. *Appl. Catal., A* **2003**, *253*, 337–358.
- (9) Su, D. S.; Maksimova, N.; Delgado, J. J.; Keller, N.; Mestl, G.; Ledoux, M. J.; Schlögl, R. *Catal. Today* **2005**, *102*, 110–114.
- (10) Cavani, F.; Trifiro, F. *Appl. Catal., A* **1995**, *133*, 219–239.
- (11) Lisovskii, A. E.; Aharoni, C. *Catal. Rev. Sci. Eng.* **1994**, *36*, 25–74.
- (12) Pereira, M. F. R.; Orfao, J. J. M.; Figueiredo, J. L. *Appl. Catal., A* **2001**, *218*, 307–318.
- (13) Keller, N.; Maksimova, N. I.; Roddatis, V. V.; Schur, M.; Mestl, G.; Butenko, Y. V.; Kuznetsov, V. L.; Schlögl, R. *Angew. Chem., Int. Ed.* **2002**, *41*, 1885–1888.
- (14) Mestl, G.; Maksimova, N. I.; Keller, N.; Roddatis, V. V.; Schlögl, R. *Angew. Chem., Int. Ed.* **2001**, *40*, 2066–2068.
- (15) Richardson, B. R.; Haw, J. F. *Anal. Chem.* **1989**, *61*, 1821–1825.
- (16) Bonardet, J. L.; Barrage, M. C.; Fraissard, J. J. *Mol. Catal. A: Chem.* **1995**, *95*, 123–143.
- (17) Meinhold, R. H.; Bibby, D. M. *Zeolites* **1990**, *10*, 121–130.
- (18) Howe, Y. Y.; Tibbetts, G. G.; Kwag, C.; Lake, M. L. *J. Mater. Res.* **2006**, *21*, 2646–2652.
- (19) Tibbetts, G. G.; Lake, M. L.; Strong, K. L.; Rice, B. P. *Compos. Sci. Technol.* **2007**, *67*, 1709–1718.
- (20) Minoux, E.; Groening, O.; Teo, K.; Dalal, S.; Gangloff, L.; Schnell, J.-P.; Hudanski, L.; Bu, I.; Vincent, P.; Legagneux, P.; Amaratunga, G.; Milne, W. *Nano Lett.* **2005**, *5*, 2135–2138.

- (21) Unalan, H. E.; Fanchini, G.; Kanwal, A.; Du Pasquier, A.; Chhowalla, M. *Nano Lett.* **2006**, *6*, 677–682.
- (22) Su, D.; Maksimova, N. I.; Mestl, G.; Kuznetsov, V. L.; Keller, V.; Schlögl, R.; Keller, N. *Carbon* **2007**, *45*, 2145–2151.
- (23) Parrott, E. P. J.; Zeitler, J. A.; Frišćić, T.; Pepper, M.; Jones, W.; Day, G. M.; Gladden, L. F. *Cryst. Growth Des.* **2009**, *9*, 1452–1460.
- (24) Jeon, G. S.; Mahan, G. D. *Phys. Rev. B* **2005**, *72*, 155415.
- (25) Saito, R.; Dresselhaus, G. *Physical Properties of Carbon Nanotubes*; Imperial College Press: London, UK, 1998.
- (26) Belin, T.; Epron, F. *Mater. Sci. Eng., B* **2005**, *119*, 105–118.
- (27) Gouadec, G.; Colombari, P. *J. Raman Spectrosc.* **2007**, *38*, 598–603.

JP811226D